NeuroImage 264 (2022) 119675

Contents lists available at ScienceDirect

NeuroImage

journal homepage: www.elsevier.com/locate/neuroimage

Improved laminar specificity and sensitivity by combining SE and GE BOLD signals

SoHyun Han[a,b,*], Seulgi Eun[a,b], HyungJoon Cho[c], Kamil Uludağ[a,b,d], Seong-Gi Kim[a,b,e,*]

[a] Center for Neuroscience Imaging Research, Institute for Basic Science (IBS), Suwon, South Korea
[b] Department of Biomedical Engineering, Sungkyunkwan University, Suwon, South Korea
[c] Department of Biomedical Engineering, Ulsan National Institute of Science and Technology, Ulsan, South Korea
[d] Techna Institute & Koerner Scientist in MR Imaging, University Health Network, Toronto, Canada
[e] Department of Intelligent Precision Healthcare Convergence, Sungkyunkwan University, Suwon, South Korea

ARTICLE INFO

Keywords:
High resolution fMRI
Ultra-high field
Layer specificity and sensitivity
Vessel-size-sensitive filter
SE BOLD

ABSTRACT

The most widely used gradient-echo (GE) blood oxygenation level-dependent (BOLD) contrast has high sensitivity, but low specificity due to draining vein contributions, while spin-echo (SE) BOLD approach at ultra-high magnetic fields is highly specific to neural active sites but has lower sensitivity. To obtain high specificity and sensitivity, we propose to utilize a vessel-size-sensitive filter to the GE-BOLD signal, which suppresses macrovascular contributions and to combine selectively retained microvascular GE-BOLD signals with the SE-BOLD signals. To investigate our proposed idea, fMRI with 0.8 mm isotropic resolution was performed on the primary motor and sensory cortices in humans at 7 T by implementing spin- and gradient-echo (SAGE) echo planar imaging (EPI) acquisition. Microvascular-passed sigmoidal filters were designed based upon the vessel-size-sensitive $\Delta R_2^*/\Delta R_2$ value for retaining GE-BOLD signals originating from venous vessels with ≤ 45 μm and ≤ 65 μm diameter. Unlike GE-BOLD fMRI, the laminar profile of SAGE-BOLD fMRI with the vessel-size-sensitive filter peaked at ~ 1.0 mm from the surface of the primary motor and sensory cortices, demonstrating an improvement of laminar specificity over GE-BOLD fMRI. Also, the functional sensitivity of SAGE BOLD at middle layers (0.75–1.5 mm) was improved by ~ 80% to ~100% when compared with SE BOLD. In summary, we showed that combined GE- and SE-BOLD fMRI with the vessel-size-sensitive filter indeed yielded improved laminar specificity and sensitivity and is therefore an excellent tool for high spatial resolution ultra-high filed (UHF)-fMRI studies for resolving mesoscopic functional units.

1. Introduction

Gradient-echo (GE) blood oxygenation level-dependent (BOLD) contrast is the most widely used technique in functional magnetic resonance imaging (fMRI) experiments due to its high sensitivity and simplicity of implementation. GE-BOLD fMRI is sensitive to deoxyhemoglobin changes, which initially occur in capillaries nearby active neurons, and drain to venules and finally to large pial veins. Thus, BOLD signal activation changes can occur as far as a few millimeters from the neuronally active site (Hillman, 2014; Lee et al., 1995; Turner, 2002). This draining problem has been recognized in the early days of fMRI research (Frahm et al., 1994; Kim SG et al., 1994; Menon et al., 1993) and may be beneficial for enhancing functional sensitivity in typical 2-3mm resolution fMRI studies. However, in sub-millimeter resolution fMRI studies, such as investigations of cortical columns and laminae, non-specific macrovascular contributions are detrimental to resolve neural functional units (De Martino et al., 2018; Dumoulin et al., 2018; Lawrence et al., 2019; Uludağ and Blinder, 2018).

Abbreviations: ASL, arterial spin labeling; BOLD, blood oxygenation level-dependent; CBF, cerebral blood flow; CBV, cerebral blood volume; CNR, contrast-to-noise ratio; CSF, cerebrospinal fluid; dSE, double spin-echo; EPI, echo planar imaging; ESP, echo spacing; fMRI, functional magnetic resonance imaging; FPM, finite perturber method; GE, gradient-echo; GRAPPA, Generalized Autocalibrating Partial Parallel Acquisition; GRASE, gradient- and spin-echo; ICV, intracortical vein; MC, Monte Carlo; M1, primary motor; RF, radiofrequency; SAGE, spin- and gradient-echo; SAR, specific absorption rate; SD, standard deviation; SE, spin-echo; SEM, standard errors of the mean; SNR, signal-to-noise ratio; S1, primary sensory; TE, echo time; TI, inversion time; TR, repetition time; tSNR, temporal SNR; VASO, vascular space occupancy; VSI, vessel size index.

* Corresponding authors at: Center for Neuroscience Imaging Research, Institute for Basic Science (IBS), Suwon, South Korea.
E-mail addresses: hansomain256@gmail.com (S. Han), seonggikim@skku.edu (S.-G. Kim).

https://doi.org/10.1016/j.neuroimage.2022.119675.
Received 26 May 2022; Received in revised form 20 September 2022; Accepted 6 October 2022
Available online 13 October 2022.
1053-8119/© 2022 The Author(s). Published by Elsevier Inc. This is an open access article under the CC BY-NC-ND license (http://creativecommons.org/licenses/by-nc-nd/4.0/)

To identify and remove macrovascular components in GE-BOLD responses, various post-processing approaches were adopted, including the use of anatomical/venographic images or BOLD characteristics such as high BOLD percent change (Fracasso et al., 2018; Kim SG et al., 1994; Olman et al., 2007; Polimeni et al., 2010; Shmuel et al., 2007), temporal delay in large veins (Goodyear and Menon, 2001; Kay et al., 2020; Lee et al., 1995; Shmuel et al., 2007), phase changes in intracortical and pial veins (Curtis et al., 2014; Menon, 2002), and hemodynamic models accounting for draining effects across layers (Havlicek and Uludağ, 2020; Heinzle et al., 2016; Markuerkiaga et al., 2016; Marquardt et al., 2018; Uludag and Havlicek, 2021). However, magnitude and dynamics of microvascular and macrovascular BOLD highly overlap (Kay et al., 2020), which makes it difficult to unambiguously separate those signals. Modeling hemodynamic signals across cortical depths from blood drainage towards pial surface is effective, but its accuracy depends on model parameters, and on heterogeneity in cortical regions and subjects. Alternatively, in the specific conditions where two stimuli (e.g., right eye vs. left eye) induce activities at the complementary territories with the similar draining effect (e.g., right vs. left ocular dominance columns), differential analysis between two stimuli can remove 'common' macrovascular contributions, and this approach was successfully applied to columnar and laminar GE-BOLD fMRI studies in humans (Cheng et al., 2001; Menon et al., 1997; Olman et al., 2012) and animals (Kim and Fukuda, 2008; Moon et al., 2007). However, this differential approach cannot be used for most fMRI studies since it is unknown whether macrovascular BOLD responses are identical for multiple stimulus conditions.

In contrast to GE-BOLD acquisition, the large vessel contribution can be significantly reduced utilizing the spin-echo (SE) BOLD approach, since a 180° refocusing pulse effectively suppresses the extravascular BOLD signal around macro-vessels (Boxerman et al., 1995; Ogawa et al., 1993; Weisskoff et al., 1994). In previous studies, SE-BOLD acquisition was observed to suppress fMRI signals in large vessels near the cortical surface when compared to GE-BOLD signals (Budde et al., 2014; Harel et al., 2006; Harmer et al., 2012; Yacoub et al., 2007; Zhao et al., 2006, 2004) and was successfully used to obtain columnar (Moon et al., 2007; Yacoub et al., 2008, 2007) and laminar fMRI (Goense and Logothetis, 2006; Harel et al., 2006; Zhao et al., 2006, 2004). Despite its high specificity to micro-vessels, SE-BOLD contrast is not widely utilized due to the overall reduced microvascular sensitivity compared to GE-BOLD contrast (Boxerman et al., 1995; Ogawa et al., 1993; Weisskoff et al., 1994). Although SE-BOLD sensitivity can be enhanced by the recently proposed double SE approach (Han et al., 2021), its application to high-resolution fMRI remains to be mostly limited by its low sensitivity.

Thus, it is highly desirable for high-resolution fMRI studies to combine the sensitivity of GE acquisition with the specificity of SE acquisition. In this study, we propose to selectively retain microvascular GE-BOLD signals by suppressing macrovascular contributions and to combine the resulting GE-BOLD signals with the SE-BOLD signals, leading to an enhancement of the spatially specific microvascular fMRI signals with high sensitivity. To that end, we apply a vessel-size-sensitive filter to the GE-BOLD signals. The filter is based on the vessel-size dependent ratio of GE and SE relaxation rates (Kiselev et al., 2005; Troprès et al., 2001) and utilized it on a voxel-by-voxel or layer-by-layer basis. In order to test this novel approach experimentally, we obtained high-resolution SE- and GE-BOLD data in humans at 7 T. Specifically, spin- and gradient-echo (SAGE) echo planar imaging (EPI) acquisition (Donahue et al., 2000, 1998; Emblem et al., 2013; Manhard et al., 2019; Schmiedeskamp et al., 2012) was adopted for 0.8 mm isotropic resolution fMRI studies of the primary sensory and motor cortices. Combined GE- and SE-BOLD fMRI with a vessel-size-sensitive filter indeed yielded improved laminar specificity and sensitivity and is therefore an excellent tool for high spatial resolution ultra-high field (UHF)-fMRI studies to resolve mesoscopic functional units.

2. Materials and methods

2.1. Simulations

2.1.1. Vascular model of cerebral cortex and re-classification of vessel types

As the BOLD contrast primarily originates from the changes of the paramagnetic deoxyhemoglobin, the spatial distribution of veins across cortical depths and on the pial surface largely determines the specificity and sensitivity of BOLD-fMRI signals. The cortical venous vasculature across the cortical depths is schematized in Fig. 1A based on (Duvernoy et al., 1981). Pial veins with a diameter of > 100 μm are connected to intracortical micro-vasculature, consisting of capillaries with an average diameter of ~ 5 μm, venules with an average diameter range of 12 μm to 36.6 μm, and intracortical veins (ICVs). Intracortical veins are further classified according to the depth of their cortical penetration; group V1 and V2 with an average diameter of 20 μm to 30 μm penetrate layers 1 to 3, group V3 with an average diameter of 45 μm to the middle of the cortex (layers 3 to 5), group V4 with an average diameter of 65 μm to lower cortical depths (layer 6), and group V5 vessels with an average diameter of 80 μm to 125 μm reaches to white matter. Group V1 to V3 often have irregular trunks and bush-like arborizations, while group V4 to V5 have straight trunks and branching venules parallel to cortical layers. Considering such vessel size distribution, all venous vessels were classified into four vessel types based on diameter: ≤ 30 μm (type 1), 30–45 μm (type 2), 45–65 μm (type 3), and > 65 μm (type 4).

2.1.2. Monte Carlo (MC) simulations

Monte Carlo (MC) simulations were performed using an in-house MATLAB (MathWorks, Natick, Massachusetts) script (Han et al., 2021) to gain insight into the extra-vascular signal properties of GE- and SE-BOLD contrast mechanisms. As at 7 T, intra-vascular contribution to the BOLD signal is small, these simulations provide a good proxy for the spatial and temporal properties of the total BOLD signal (Uludağ et al., 2009). In short, three-dimensional binary matrices for vascular structure were generated using randomly oriented cylinders. The susceptibility difference between blood and tissue for fully deoxygenated blood was set to $\Delta\chi = 0.11$ ppm in cgs units (Jain et al., 2012; Spees et al., 2001). A susceptibility difference value of (1-Y) × 0.11ppm = 0.011ppm was used, with resting-state Y = 60% and activation Y = 70%. The finite perturber method (FPM) was used to calculate the magnetic field shift from the BOLD effect (Pathak et al., 2008) resulting from an applied field strength of B_0 = 7 T. In the FPM, the magnetic field shift by an arbitrary structure is calculated as the sum of the magnetic field shifts by uniformly packed small perturbers within the structure. Initially, 2×10^5 proton spins outside of the cylinders were positioned randomly and moved in a random trajectory with a diffusion time step of 0.2 ms and a diffusion coefficient of 10^{-5}cm^2/s. The vessel diameter was varied from 2μm to 200μm at a fixed V_b of 3%, with V_b representing the mean blood volume (Báez-Yánez et al., 2017; Spees et al., 2001). Echo times (TEs) for GE and SE were set as 18ms and 58ms, respectively, matching experimental conditions.

2.1.3. Vessel-size-sensitive filters

Our idea is to generate a vessel-size-sensitive filter function (i.e., parameterized by exponent alpha (α)), and then apply it to GE-BOLD signals to suppress macrovascular contributions in the GE-BOLD signals and to retain microvascular contributions. Filtered GE-BOLD and SE-BOLD data are combined using $S_{SAGE} = (S_{GE})^{\alpha} \times (S_{SE})$ on a voxel-by-voxel or layer-by-layer basis at each time point. This process is essentially identical to SAGE-BOLD % change = α × (GE-BOLD % change) + (SE-BOLD % change) as shown in Supplementary Fig. S1.

Since $\Delta R_2^*/\Delta R_2$ increases with vessel diameter and is often used as a vessel size index (Kiselev et al., 2005; Troprès et al., 2001), a vessel-size-sensitive filter function was generated by utilizing $\Delta R_2^*/\Delta R_2$. A

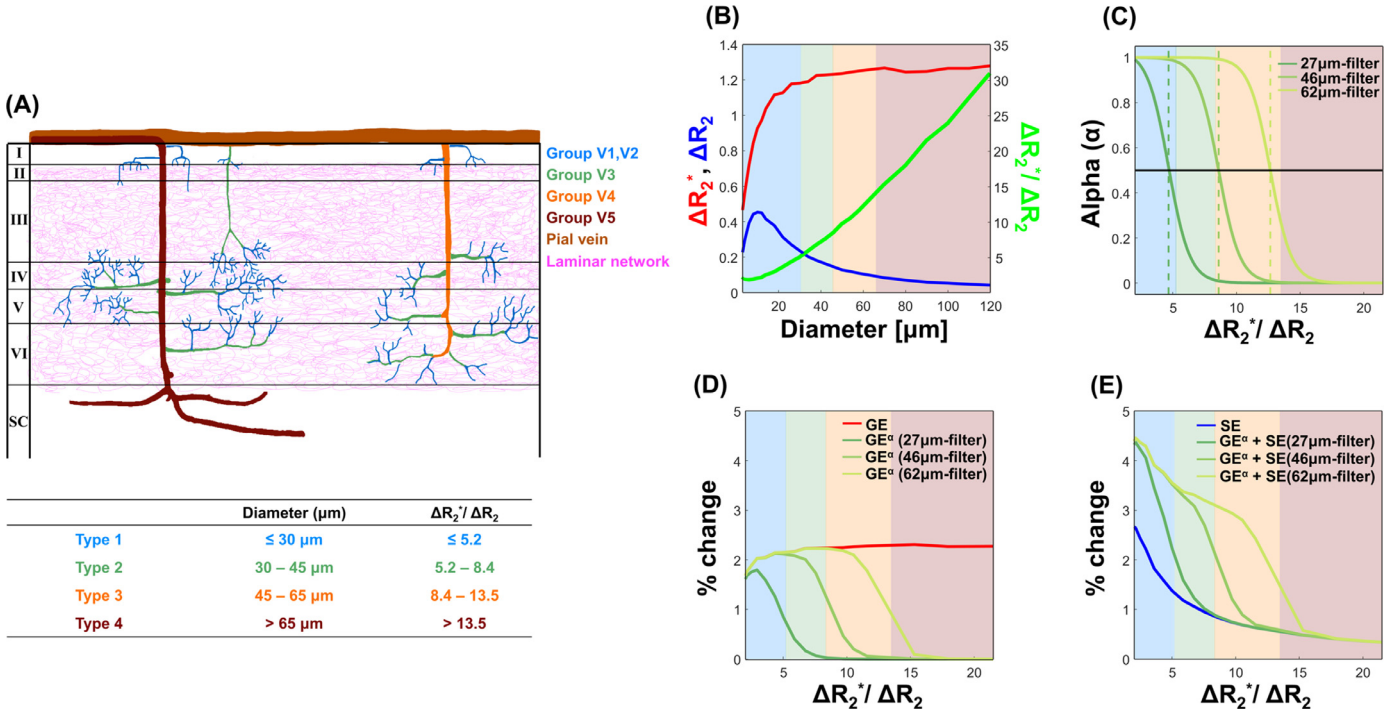

	Diameter (μm)	$\Delta R_2^*/\Delta R_2$
Type 1	≤ 30 μm	≤ 5.2
Type 2	30 – 45 μm	5.2 – 8.4
Type 3	45 – 65 μm	8.4 – 13.5
Type 4	> 65 μm	> 13.5

Fig. 1. Cortical venous vasculature and vessel-size-sensitive filters. (A) The cortical venous vasculature across the cortical depths in humans, drawn based on Fig. 27 in Duvernoy et al (1981). Note that arteries are not considered because their contribution to the BOLD signal at high fields is negligible. Venous vessel classification into four vessel types based on diameter: ≤ 30μm (type 1), 30–45 μm (type 2), 45–65 μm (type 3), and > 65 μm (type 4). The corresponding $\Delta R_2^*/\Delta R_2$ values for each vessel type are listed in the table below. For Monte Carlo susceptibility simulations, gradient echo time was 18 ms and spin echo time was 58 ms at 7 T. **(B)** ΔR_2^*, ΔR_2 and $\Delta R_2^*/\Delta R_2$ plots as a function of vessel diameter as red, blue, and green colored lines, respectively. $\Delta R_2^*/\Delta R_2$ almost linearly increases with vessel diameter. **(C)** Three sigmoidal shaped low-pass filters for selectively filtering ≤ 30 μm (type 1), < 45 μm (type 1-2), and < 65 μm (type 1-3), and named to reflect the vessel diameter where alpha becomes 0.5 as 27 μm-, 46 μm-, and 62 μm-filters, respectively. **(D)** Percent changes of GE BOLD (red) and vessel-size-sensitive filtered GE BOLD (GE^{α}) with three filters as a function of vessel-size-sensitive $\Delta R_2^*/\Delta R_2$. **(E)** Percent changes of SE BOLD (blue) and combined SE and filtered GE BOLD (GE^{α}) with three filters as a function of vessel-size-sensitive $\Delta R_2^*/\Delta R_2$. Blue, green, orange, and red background-colored zones are corresponding to vessel type 1 to 4, respectively.

low-pass filter was designed using a sigmoid function:

$$\alpha = 0.5 - 0.5 \times \tanh\left(0.6 \times (D - D_{1/2})\right)$$
$$= 0.5 - 0.5 \times \tanh\left(0.6 \times (\Delta R_2^*/\Delta R_2 - (\Delta R_2^*/\Delta R_2)_{1/2})\right),$$

where D is the $\Delta R_2^*/\Delta R_2$ of individual voxel, $D_{1/2}$ is the $\Delta R_2^*/\Delta R_2$ to reduce the original GE signals as $S_{GE}^{0.5}$. α is ~1 at D << $D_{1/2}$, 0.5 at D = $D_{1/2}$, and ~0 at D >> $D_{1/2}$. Three filters were designed to have $D_{1/2}$ to correspond to a diameter of 27 μm, 46 μm, and 62 μm (estimated by green line in Fig. 1B) for selectively low-pass filtering ≤ 30 μm (type 1), < 45 μm (type 1-2), and < 65μm (type 1-3), respectively. The filters are named to reflect the vessel diameter, for which the alpha is equal to 0.5. The transition slope of 0.6 was chosen to have our desired transition diameter range, which corresponds to alpha value of 0.9–0.1 at a diameter of 15–36 μm for the 27 μm-filter, 38–53 μm for the 46 μm-filter, and 55–68 μm for the 62 μm-filter. Note that alpha ranges as > 0.9 and < 0.1 represent pass and rejection vessel diameters. For example, the purpose of the 27 μm-filter was to enhance only vessel type 1 and suppressed larger vessel types with a rejection diameter (α < 0.1) of 36 μm as shown in Fig. 1C.

2.2. Experiments

2.2.1. Participants and MRI system

Ten healthy subjects (6 male and 4 female) aged 25–35 years old participated in this study, approved by the Institutional Review Board of Sungkyunkwan University. Procedures were fully explained to all subjects, and informed written consent was obtained before scanning in accordance with the Declaration of Helsinki. All measurements were performed on a 7 T scanner (MAGNETOM Terra, Siemens Healthineers, Erlangen, Germany) equipped with a single channel transmitter and a 32 channel receive head coil (NOVA Medical, Wilmington, MA). The movement of the subjects was minimized by tightly padding the space inside the coil with MR compatible cushions.

2.2.2. Implementation of Spin- and gradient-echo (SAGE) EPI and reconstruction

A schematic diagram of the SAGE-EPI sequence is shown in Supplementary Fig. S2A. Please note that the SAGE EPI is unrelated to the gradient- and spin-echo (GRASE) sequence (Oshio and Feinberg, 1991). To achieve high spatial resolution laminar fMRI by overcoming the spatial encoding limitations of single-shot EPI, multi-shot segmented EPI was used. The *k*-space data were reconstructed by applying the sliding-window concept to maintain temporal resolution with shot repetition times (Han et al., 2021) using an in-house MATLAB (MathWorks, Natick, Massachusetts) script. As an example, 3 shots were merged in this study using a sliding-window, and for the second time frame, TR_{shot} (2), TR_{shot} (3), and TR_{shot} (4) were used for the image reconstruction instead of using TR_{shot} (4), TR_{shot} (5), and TR_{shot} (6); TR_{shot} is each shot's repetition time as shown in Supplementary Fig. S2B. Nyquist ghost correction and phase offset correction were performed independently for each shot. Conventional Generalized Autocalibrating Partial Parallel Acquisition (GRAPPA) reconstruction was performed after merging three shots as well.

2.2.3. Experimental session setup and image acquisition

To demonstrate enhanced sensitivity and specificity in the microvascular region of the SAGE-BOLD signal at 0.8 mm isotropic resolution,

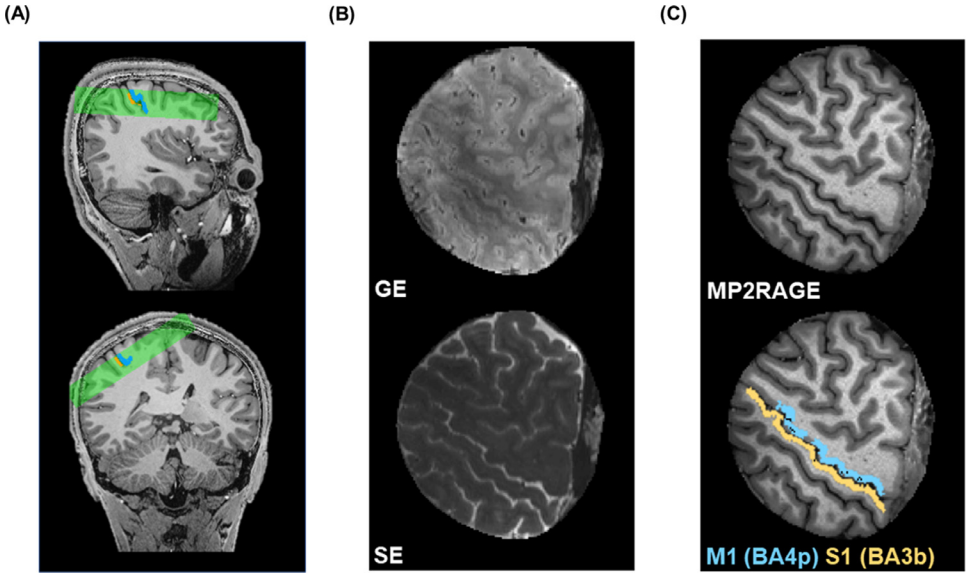

Fig. 2. Slice selection and SAGE-EPI implementation. (A) Oblique slices aligned perpendicular to the central sulcus between M1 and S1 as depicted in green box. **(B)** GE- and SE-EPI images from the implemented SAGE-EPI sequence. **(C)** Co-registered MP2RAGE images onto EPI images. The masks of primary motor (M1) and sensory (S1) cortices with blue and yellow colors, respectively.

we selected regions of the human primary motor (M1) and sensory (S1) cortices proximal to the central sulcus (Han et al., 2021; Huber et al., 2020, 2017, 2015), as shown in Fig. 2A. Slices were aligned perpendicular to the participants' central sulcus between M1 and S1. Subjects underwent a 3.8min unilateral (left-hand) fist-clenching and touching task paradigm (initial 20 s resting followed by 8 blocks of alternating 6 s clenching and 20 s resting). With an update rate of 2 s by the sliding-window approach, a total of 114 images for each run were obtained (i.e., 10 resting – [3 stimulation – 10 resting] × 8 images), and 10 runs were acquired in total to ensure sufficient sensitivity of SE-BOLD contrast.

The imaging parameters for multi-shot SAGE EPI were as follows: 0.8 × 0.8 mm^2 in-plane resolution, $R_{in\text{-}plane}$ = 9 (for each shot; effective $R_{in\text{-}plane}$ = 3 by 3 shots), field of view (FOV) = 120 × 120 mm^2, 24 slices (slice thickness = 0.8 mm), flip angle pair = 90–180°, partial Fourier = 6/8, echo spacing (ESP) = 1 ms (1282 Hz/Px), repetition time (TR) of each shot = 2000 ms, TE_{GE} / TE_{SE} = 18 / 58 ms. Note that the EPI readout per shot was 12ms, which is close to optimal values for a readout window of about 0.5 × T_2^* to reduce T_2^* contamination (Goense and Logothetis, 2006). To acquire a B_0 field map for distortion correction of the EPI images, FLASH images with the same imaging parameters as the SAGE EPI were acquired, except for bandwidth = 620 Hz/Px, TEs = 3.3, 6.3 ms, and flip angle = 50°. Anatomical images were acquired using the MP2RAGE sequence (Marques et al., 2010) with imaging parameters: sagittal orientation, 0.7 mm isotropic resolution, FOV = 224 × 210 × 168 mm^3, $R_{in\text{-}plane}$ = 3, inversion times (TIs) = 1.0 / 3.2s, TE = 2.29 ms, TR = 4500 ms, readout bandwidth = 200 Hz/Px, and flip angle = 4°.

2.3. Data analysis

2.3.1. Preprocessing and functional analysis

Functional images were motion-corrected using SPM12 (Functional Imaging Laboratory, University College London, UK) with 6 motion parameters. All runs after motion correction were registered and concatenated. The distortion of the EPI images was corrected with the B_0 field map from the FLASH sequence, performed with PRELUDE and FUGUE from the FSL package (http://www.fmrib.ox.ac.uk/fsl). The anatomical MP2RAGE images were then co-registered onto motion and distortion corrected functional images using SPM12 as shown in Fig. 2C. The masks of primary motor (M1) and sensory (S1) cortices were generated by using FreeSurfer (http://surfer.nmr.mgh.harvard.edu/) as shown in Fig. 2C. From the anatomical images, cerebrospinal fluid (CSF), gray matter, and white matter were visually identified, which enabled the generation of layer masks registered onto the functional images. All other data analyses, such as calculation of percent signal change, sensitivity, specificity indices, and contrast-to-noise ratio (CNR) were performed using custom-written MATLAB scripts (MathWorks, Natick, MA, USA). Statistical analysis was done using FSL FEAT (Worsley, 2001) from the FSL package using standard parameter settings without spatial smoothing. The percentage signal change was calculated on the average 8 blocks of stimulation and rest; the rest signal was averaged over 6s before the onset of the task, whereas the evoked signal was averaged over 6 s, excluding the initial 4s right after the stimulus onset to minimize the influence of onset transient changes.

2.3.2. Characterization of SAGE-BOLD signal

To characterize the SAGE-BOLD signal (shown in Supplementary Fig. S3), 1) GE-BOLD z-score map was thresholded with a z-value of ≥ 1.5 and multiplied by M1 and S1 masks. 2) Corresponding $\Delta R_2^*/\Delta R_2$ values were calculated as $\Delta R_2^* = -\ln(S_{GE,task}/S_{GE,rest}) / TE_{GE}$ and $\Delta R_2 = -\ln(S_{SE,task}/S_{SE,rest}) / TE_{SE}$ where subscript task and rest indicates the task and rest periods, respectively. Each activated voxel was assigned to correspond to a vessel type (i.e., type 1 to 4) as explained in Materials and Methods 2.1.1. 3) Voxel-wise or layer-wise alpha value was applied to GE-BOLD data (S_{GE}), and SAGE-BOLD responses were computed from $S_{GE}{}^{\alpha} \times S_{SE}$ timeseries. 4) The number of activated voxels, time courses, percent signal changes, and z-score values across ten subjects were calculated for each vessel type. Voxel-wise calculations of percent signal changes and z-score values were performed, and mean values for each vessel type were extracted from each subject. After that, the mean and standard deviation of those values for ten subjects were calculated. 5) The specificity index was calculated as the percent signal change values ($P_{each\ type}$) normalized to that of the largest vessel-size type 4 (P_{type4}) in each BOLD contrast to quantitatively measure the improvement of specificity. For example, the percent signal change in vessel type 2 (P_{type2}) is the combination of microvascular and macrovascular contributions, which can be expressed as $P_{type2} = f_{type2} \times P_{microvessel} + (1\text{-}f_{type2}) \times P_{macrovessel}$, where f_{type2} is the microvascular fraction in vessel type 2. With the assumption that P_{type4} is dominated by macro-vessels ($P_{type4} \approx P_{macrovessel}$), the ratio $P_{type2} / P_{type4} \approx f_{type2} \times (P_{microvessel} / P_{macrovessel}) + (1\text{-}f_{type2})$ reflects the relative contribution of microvasculature compared to macro-vessels ($P_{microvessel} / P_{macrovessel}$); the value of 1.0 indicates equal contributions of micro- and macro-vasculature, < 1.0 for less microvascular contribution, and > 1.0 for higher microvascular contribution. 6) The sensitivity index was calculated as z-scores normal-

ized to that of reference SE-BOLD fMRI to investigate the improvement of sensitivity compared to SE BOLD.

2.3.3. Laminar profile

Anatomical T_1-weighted images from the MP2RAGE sequence were used to delineate white matter and CSF borders for the laminar analysis. To generate a cortical-depth mask, we upsampled the images 4 times with cubic interpolation (i.e., 200 μm in-plane resolution), and manually delineated the gray matter boundaries with white matter and CSF on the anterior and posterior banks of the central sulcus, including the hand knob region of M1 and S1. For quantitative analyses, layers were drawn in both M1 and S1 regions, where task-responsive activation was observed (please see illustration of M1 and S1 masks in Supplementary Fig. S3D). Since the thickness of human M1 is approximately 4 mm (Fischl and Dale, 2000) and the thickness of S1 is about half of that of M1 (Huber et al., 2015), the cortex was divided into 20 and 10 equidistant depths for M1 and S1 areas, respectively. Then, cortical depths were determined using the software suite LAYNII (Huber et al., 2017, 2015). After creating layers for each slice, the slices-averaged laminar profile was calculated to improve statistical power and minimize bias in single-slice selection.

Percent signal changes were calculated for each layer, and $\Delta R_2^*/\Delta R_2$ was calculated to assign a α value. Z-score values for each layer were calculated with $S_{SAGE,\ layer} = (S_{GE,\ layer})^{\alpha,layer} \times (S_{SE,\ layer})$. Note that only layers with z-score level of SE BOLD above 2.58 (99% confidence level, p-value < 0.01) was considered as activated layers and the percent signal change, z-score value, and $\Delta R_2^*/\Delta R_2$ of the valid layers were calculated and plotted. To quantitatively evaluate noise propagation by combined SE- and GE-BOLD processing, noise level was calculated as standard deviation divided by mean of the initial rest signals from 4 to 16 s in each layer. Also, CNR was calculated using the following equation for each layer, CNR = ΔS / σ where ΔS is the averaged signal difference of 8 blocks between stimulation and rest periods (Section 2.3.1), and σ is the standard deviation of the initial rest signal. To quantify specificity and sensitivity indices in laminar profile, three cortical depths were defined: superficial (0–0.75 mm), middle (0.75–1.50 mm), and deep (1.50–2.25 mm).

3. Results

3.1. Simulations for designing vessel-size-sensitive filters of GE BOLD

MC simulations provide the extravascular BOLD sensitivity as a function of vessel size (Fig. 1B). Similar to previous MC simulation studies (Boxerman et al., 1995), GE-BOLD sensitivity (ΔR_2^*) increases with vessel diameter and reaches a plateau for diameters larger than ~ 30 μm, while SE-BOLD sensitivity (ΔR_2) peaks at ~ 8μm diameter and decreases for larger vessel size. In addition, ΔR_2^* values are typically larger than ΔR_2 values. As a result, GE BOLD has high sensitivity, but poor specificity to microvessels, whereas SE BOLD has high specificity to microvessels, but low sensitivity. Even for highly specific type 1 vessel (blue color zone), the overall SE-BOLD sensitivity is lower than that of GE BOLD. $\Delta R_2^*/\Delta R_2$ (green) value is almost linearly related to vessel diameter and is therefore considered as vessel size index (VSI). Then, three alpha filters of GE-BOLD signals were designed using the sigmoid curves as a function of $\Delta R_2^*/\Delta R_2$ as shown in Fig. 1C.

Resulting vessel-size-sensitive changes in filtered GE BOLD (GE^{α}) with TE of 18ms were shown along with the original GE-BOLD response (red) in Fig. 1D. The 27 μm-filter (dark green line) suppresses signal of vessel types 2–4; the 46 μm-filter of vessel types 3–4, and the 62 μm-filter (bright green line) of vessel type 4. Microvascular SE-BOLD signals with TE of 58 ms (blue) were combined with three microvascular-filtered GE BOLD responses for SAGE BOLD responses (Fig. 1E). SAGE BOLD signal with the 27 μm-filter has higher sensitivity for vessel type 1 compared to that of SE BOLD. For 46 μm- and 62 μm-filters, the signal enhancement was extended to vessel type 2 and vessel type 2 - 3, respectively.

3.2. Characterization of experimental SAGE-BOLD fMRI

To investigate the benefit of combined SE- and filtered GE-BOLD fMRI at 7 T, laminar BOLD fMRI with 0.8 mm isotropic resolution was acquired in human sensory and motor cortices with unilateral (left-hand) fist-clenching and touching task paradigm (Fig. 2A). Anatomical contrasts between CSF and gray matter are well visualized in SE EPI, and between gray matter and white matter in GE EPI (Fig. 2B). Interestingly, the CSF signal was suppressed in the GE-EPI image with short TR, because CSF T_1 is relatively long compared to T_1 in white matter and gray matter. When TR was set to 10 s, the CSF signal became large in the GE-EPI image compared to the CSF signal with TR of 2s (Supplementary Fig. S4).

Percent change maps of GE- and SE-BOLD fMRI were obtained from the statistically active voxels in the GE-BOLD fMRI and overlaid on the original images (Fig. 3A for one representative subject). Voxel-wise $\Delta R_2^*/\Delta R_2$ values were calculated (Fig. 3A, 3rd row) and its histogram was obtained (Fig. 3B). Each voxel was classified as one of four vessel types (blue, green, orange, and red colors in 4th row of Fig. 3A and Fig. 3B), based on their $\Delta R_2^*/\Delta R_2$ values. Distribution of active voxels for each vessel type (mean ± standard error of mean (SEM), n = 10 subjects) was plotted in Fig. 3C. Most active voxels belonged to the category of vessel type 1–2, which was associated with a laminar vascular network (diameter ≤ 30 μm). Vessel type 3 (orange) and type 4 (red) accounted for ~ 20% of the total active voxels (Fig. 3C), being mostly located in the CSF containing the large draining veins (the white arrows in Fig. 3A). Contribution of these macrovascular voxels degrades spatial specificity and should be minimized in high-resolution fMRI studies.

3.3. Functional specificity and sensitivity of combined SE- and GE-BOLD fMRI signals

To investigate the effect of the filter functions on combined SE- and GE-BOLD fMRI, voxel signals were averaged to obtain the time course for each vessel type. The mean fMRI responses of GE-, SE-, and SAGE-BOLD with three filters (n = 10 subjects) are shown in Fig. 4A. As expected, the highest percent changes were observed from vessel type 4 for GE BOLD, whereas for SE BOLD, the vessel type 1 had the highest responses. For SAGE BOLD with all three filters, significant enhancements of percent signal change were observed from vessel type 1. Additionally, the 46μm-filter enhanced signals from vessel type 2, and the 62 μm-filter enhanced BOLD signals from both vessel types 2 and 3. In all three filters, responses from the vessel type 4 were suppressed. These experimental SAGE-BOLD fMRI percent changes with three different filters are consistent with the corresponding MC simulations (Fig. 1E). The mean percent signal changes of SAGE BOLD with three filters were higher than those of GE and SE BOLD, especially for type 1 (Fig. 4B; mean ± standard deviation (SD), n = 10). To quantitatively investigate the improvement of sensitivity, z-score values were obtained from GE-, SE-, and SAGE-BOLD fMRI with the three filters (Fig. 4C; mean ± SD, n = 10). For all three filters, the overall z-score values of SAGE BOLD were improved compared to those of SE BOLD. Then, specificity and sensitivity indices are plotted in Fig. 4D and 4E, respectively. To better visualize sensitivity gain of type 1 and 2 vessels by SAGE-BOLD signals, the bar plots in Fig. 4E were rearranged in the Inset. Table 1 also tabulates vessel-type-wise specificity and sensitivity indices. The 27 μm-filter preferentially increased both specificity and sensitivity for vessel type 1; the 46 μm-filter for vessel types 1 and 2; and the 62 μm-filter for vessel types 1–3. As an example, for the 46μm-filter, specificity index of vessel types 1 and 2 was ~ 6 and that of vessel type 3 was 2.63, which means that the 46μm-filter enhances the specificity selectively for vessel types 1 and 2. And sensitivity indices with SAGE approach for all three filters shows

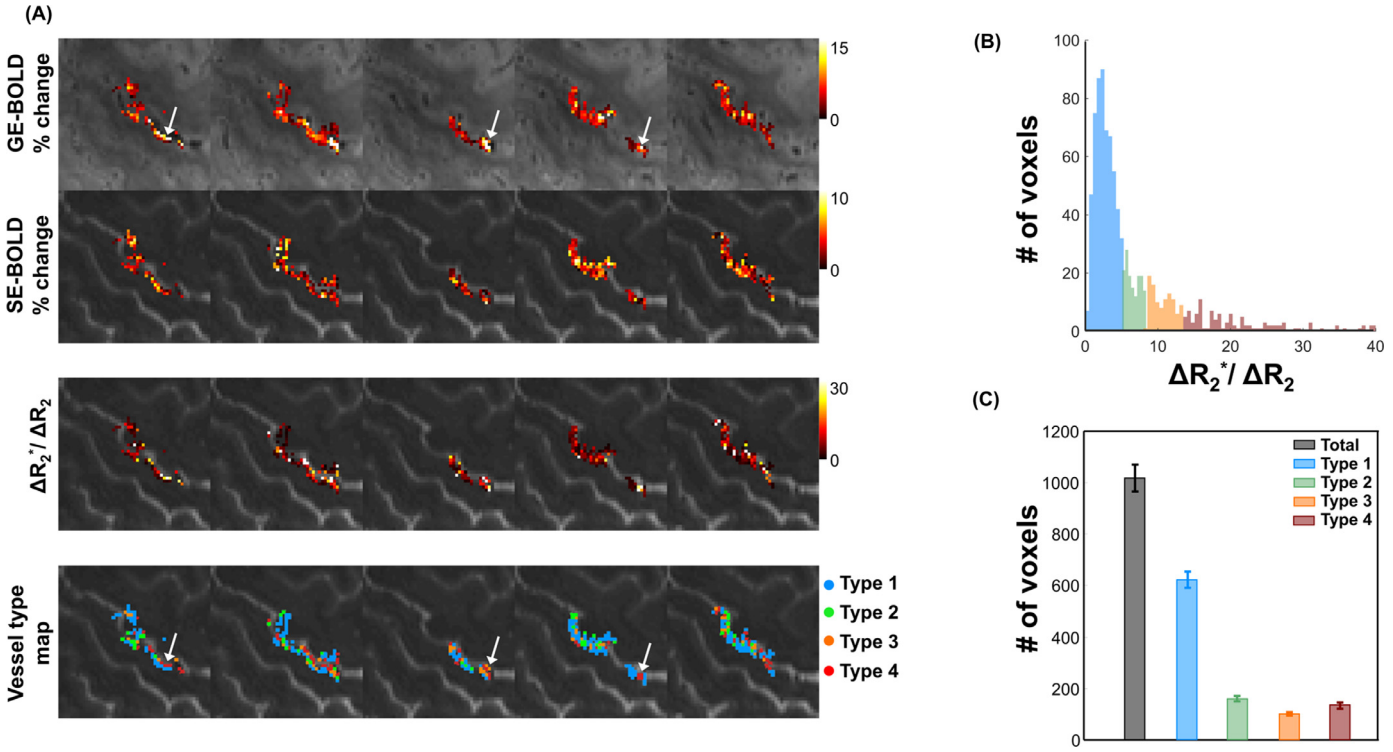

Fig. 3. Classification of active voxels in M1 and S1 to vessel type. (A) Percent change maps of GE- and SE-BOLD, $\Delta R_2^*/\Delta R_2$ value and vessel type maps (one representative subject, five representative slices). White arrows indicate high GE-BOLD changes in the CSF area. **(B)** Distribution of number of activated voxels as a function of $\Delta R_2^*/\Delta R_2$ (one representative subject data in (A)). Four vessel types represent in blue, green, orange, and red colors. **(C)** The number of activated voxels of total (black), and four vessel types (mean and SEM, $n = 10$ subjects).

Table 1
Specificity and sensitivity indices for vessel types (mean ± SD, $n = 10$ subjects)[a].

Specificity index[b]	[Type 1] / [type 4]	[Type 2] / [type 4]	[Type 3] / [type 4]
GE	0.42 ± 0.07	0.63 ± 0.10	0.79 ± 0.12
SE	4.38 ± 0.60	2.45 ± 0.32	1.91 ± 0.25
SAGE 27 μm-filter	6.25 ± 0.87	2.83 ± 0.38	1.92 ± 0.25
SAGE 46 μm-filter	6.76 ± 0.92	5.79 ± 0.80	2.63 ± 0.42
SAGE 62 μm-filter	6.25 ± 0.76	5.88 ± 0.76	5.56 ± 0.65

Sensitivity index[c]	Type 1	Type 2	Type 3	Type 4
GE	1.03 ± 0.04	2.06 ± 0.03	3.27 ± 0.04	8.65 ± 0.40
SE	1	1	1	1
SAGE 27 μm-filter	1.35 ± 0.02	1.65 ± 0.04	1.73 ± 0.08	2.15 ± 0.17
SAGE 46 μm-filter	1.38 ± 0.03	1.84 ± 0.04	2.24 ± 0.08	3.13 ± 0.20
SAGE 62 μm-filter	1.38 ± 0.03	1.87 ± 0.04	2.40 ± 0.08	3.84 ± 0.15

[a] Voxel-wise $\Delta R_2^*/\Delta R_2$ value was used for defining vessel type of each active voxel; Type 1 for ≤5.2, Type 2 for 5.2-8.4, Type 3 for 8.4-13.5, and Type 4 for >13.5. Gradient-echo (GE), spin-echo (SE), spin and gradient echo (SAGE) BOLD with three different vessel-size filters were evaluated.

[b] Specificity was determined by percent changes divided by that of Type 4; the higher is more specific to microvessels.

[c] Sensitivity index was calculated by z-scores normalized by that of SE BOLD in each corresponding vessel type.

larger than 1, which means that SAGE BOLD enhanced the sensitivity compared to SE BOLD.

3.4. Laminar profile of SAGE-BOLD with different vessel-size-sensitive filters

To investigate the laminar profile of SAGE BOLD, the cortical depth profiles of GE-BOLD, SE-BOLD, and SAGE-BOLD fMRI using the three filters were obtained from sensory and motor cortices by averaging the iso-depth signals from each subject's activated slices ($n = 10$ subjects). Laminar profiles of $\Delta R_2^*/\Delta R_2$, percent signal change, z-score, specificity index, and sensitivity index in the M1 and S1 regions are plotted in Fig. 5 and Fig. 6, respectively (mean and SEM, $n = 10$ subjects). The vessel size index and GE-BOLD fMRI are largest at the cortical surface, where the concentration of draining vessels is high and decreases monotonically with increasing cortical depth. In contrast, for SE BOLD and SAGE BOLD using all three filters, the z-score levels decrease at the cortical surface and peak in the gray matter for both M1 and S1.

SAGE-BOLD fMRI using the 27 μm-filter showed a cortical profile pattern similar to that of SE BOLD (Fig. 5B-C and Fig. 6B-C), since

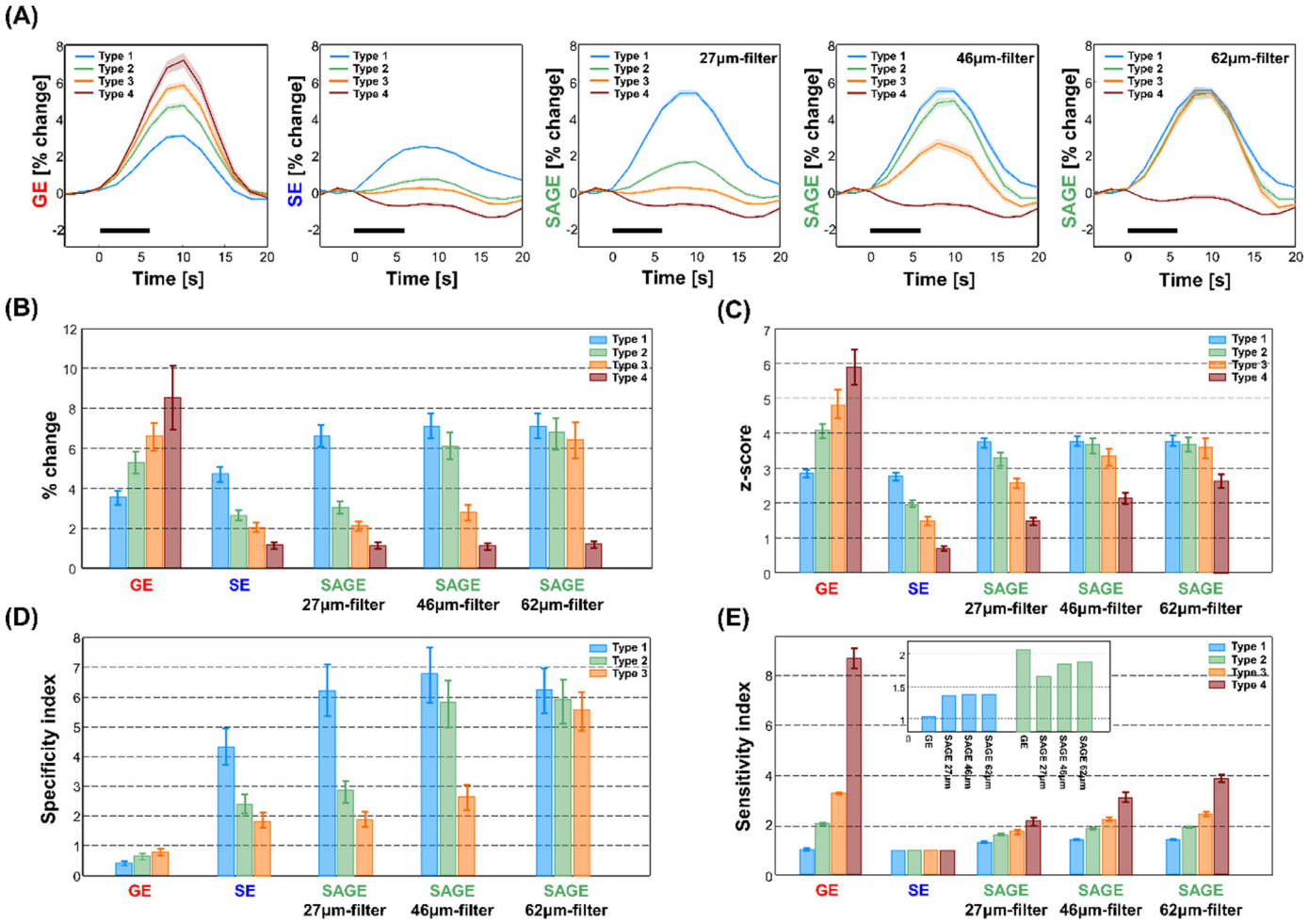

Fig. 4. Characteristics of GE-, SE- and SAGE-BOLD signals with three vessel-size-sensitive filters. (A) The mean fMRI responses of GE-, SE-, and SAGE-BOLD with three filters for each vessel type. The solid and shaded lines show the mean and SEM across 10 subjects. The bar graph (mean and SD, n = 10 subject) of **(B)** percent signal changes, **(C)** z-score levels, **(D)** specificity index, and **(E)** sensitivity index in four vessel types. Specificity index was calculated by the percent change of each vessel type divided by that of vessel type 4 in each imaging modality. GE-BOLD data has poor specificity (less than 1), while SAGE increases specificity. Sensitivity index was calculated by z-score value of each vessel type in each imaging modality normalized by that of SE BOLD. To better compare the sensitivity index across different BOLD contrasts, vessel types 1-2 were shown in Inset. Sensitivity of SAGE with the 46-μm filter was close to that of GE BOLD for vessel types 1-2 (< 45 μm diameter).

laminar $\Delta R_2^*/\Delta R_2$ values belonged to type 2-3 (light blue to light yellow band in Fig. 5A and Fig. 6A). The 62 μm-filter enhanced cortical sensitivity broadly, while maintaining the general GE-BOLD cortical profile. SE- and SAGE-BOLD fMRI with all three filters peaked at about 0.8 and 1.0mm depth from the cortical surface in M1 and S1, respectively. The peak in M1 is located at the upper cortical lamina (~ 0.8 mm), which agrees well with the corresponding double spin-echo (dSE) EPI and cerebral blood volume (CBV)-weighted vascular space occupancy (VASO) responses (Han et al., 2021; Huber et al., 2020). Note that the lateral side of the hand knob in the M1 area has been shown to exhibit double-peaks in laminar profile (Huber et al., 2017). In contrast, we did not observe the double-peaks. This is possibly due to the slice coverage, which focused on the inner part of central sulcus, and may not fully or partly have included the lateral side of the hand knob as shown in Fig. 2A. The peak in S1 is located at the middle cortical layer (~ 1.0 mm), which is also consistent with VASO-fMRI and dSE EPI (Han et al., 2021; Yu et al., 2019). It is known that the highest microvascular density is reported in middle cortical layers of humans (Duvernoy et al., 1981) and especially capillary density is higher in layer 4 in the rodent somatosensory cortex (Blinder et al., 2013; Lee et al., 2022; Masamoto et al., 2004), which corresponded to the local peaks for SE and SAGE laminar profiles in this study.

To quantify spatial specificity, sensitivity gains and CNR, the laminar specificity was calculated as the percent signal change of the middle (0.75–1.50 mm) and deep cortical layer (1.50–2.25 mm) normalized by that of the superficial layer (0–0.75 mm), and the sensitivity index was determined as z-scores normalized to that of SE-BOLD fMRI. Cortical depth-dependent specificity and sensitivity indices are plotted for M1 and S1 area (Fig. 5D-E and Fig. 6D-E) and listed in Table 2. SAGE-BOLD with the 46 μm-filter has the highest specificity in the middle and deep cortical layers compared to other BOLD imaging contrasts. Sensitivity increases with larger-diameter filter; the 46μm-filter increased ~80% sensitivity gain in the middle cortex relative to SE BOLD. Overall, the CNR of SAGE with the three filters is higher than that of SE but lower than GE, and the pattern of CNR has a similar tendency to the sensitivity index.

3.5. *Improved laminar mapping by SAGE-BOLD with an optimized vessel-size-sensitive filter*

Finally, the z-score maps of GE-, SE-, and SAGE-BOLD with the 46 μm-filter were compared to determine the suitability of the different approaches for BOLD laminar mapping at 7 T. Fig. 7 shows representative slices of ten subjects. Anatomical T_1-weighted images (MP2RAGE)

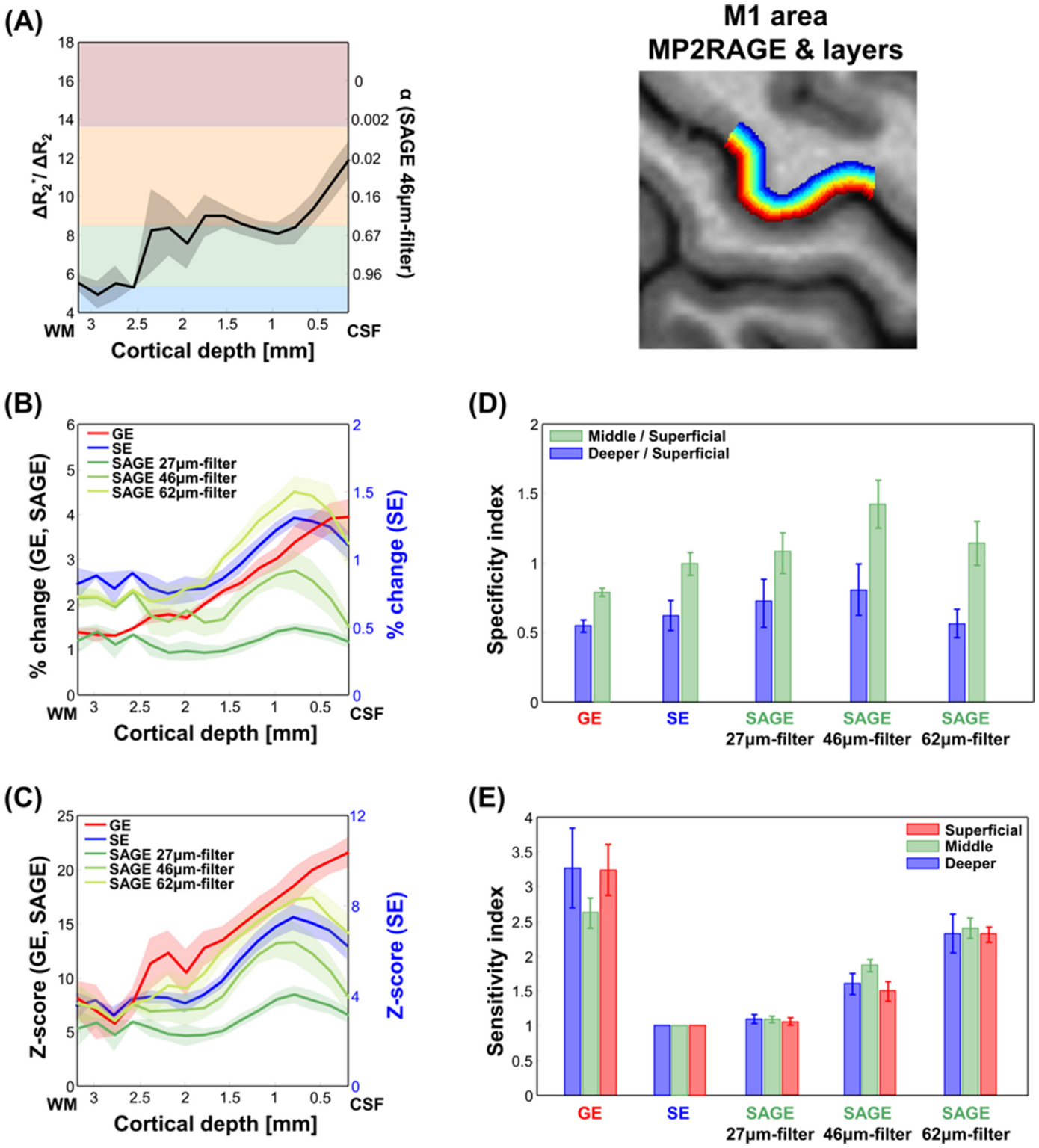

Fig. 5. Motor cortical profiles of SAGE with vessel-size-sensitive filters versus GE and SE BOLD. Laminar profiles of **(A)** $\Delta R_2^*/\Delta R_2$, **(B)** percent signal change, **(C)** z-score level, **(D)** specificity index, and **(E)** sensitivity index in the M1 region obtained from GE-, SE-, and SAGE-BOLD with three filters. Layer ROIs were obtained from GE-BOLD z-score maps in Supplementary Fig. S3D, and only single-slice iso-depth ROIs were shown. For specificity and sensitivity indices, error bar shows SEM. Solid and shaded lines are mean and SEM across ten subjects. GE BOLD showed the largest sensitivity at the cortical surface, whereas SE and SAGE BOLD using showed the largest sensitivity at ~ 0.8 mm depth, corresponding to the previous studies. For better visualization, the SE BOLD profile was plotted in a different scale. The 46 μm-filter appears to be a good comprise of sensitivity and specificity gain.

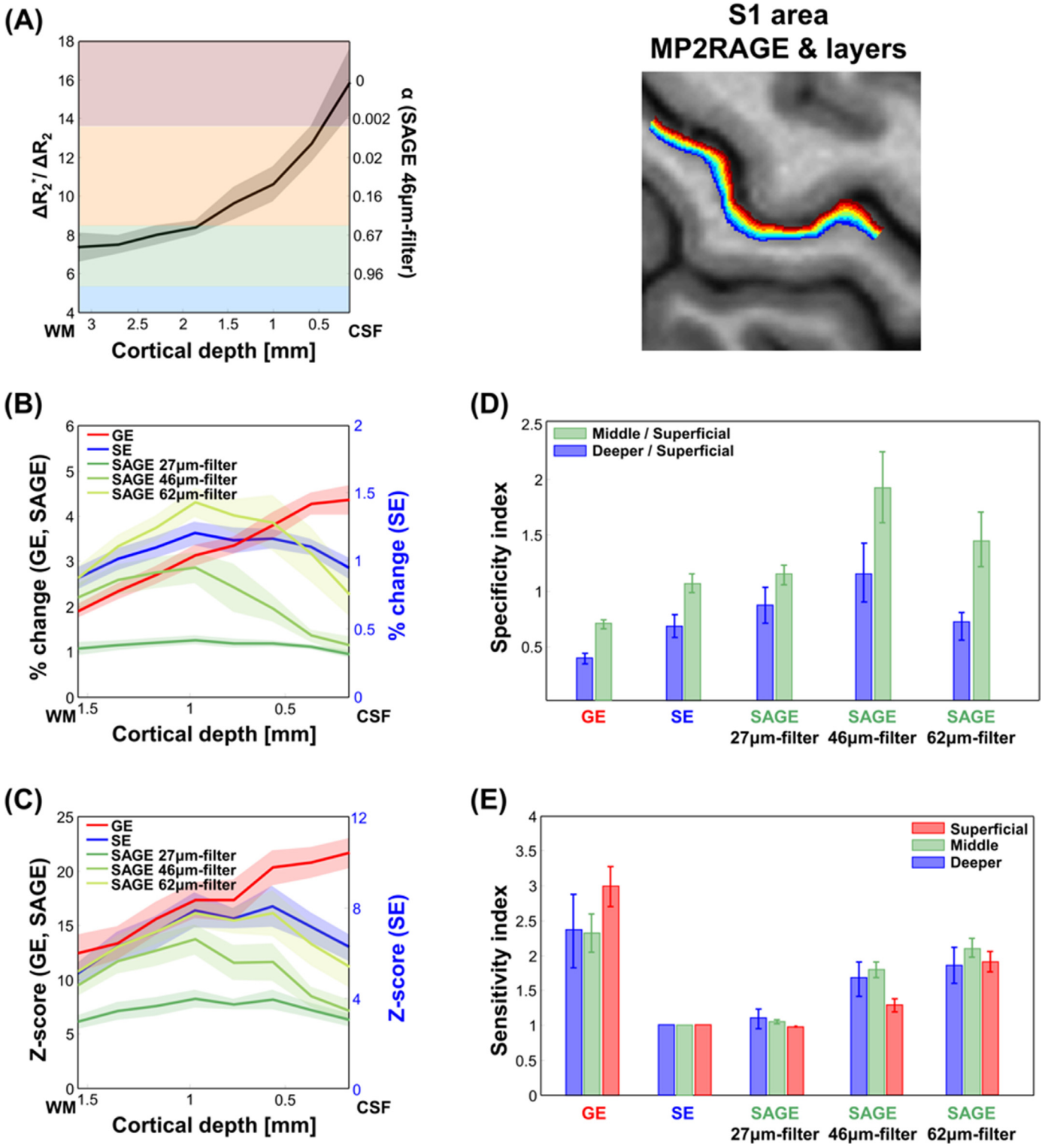

Fig. 6. Sensory cortical profiles of SAGE with vessel-size-sensitive filters versus GE and SE BOLD. Laminar profiles of **(A)** $\Delta R_2^*/\Delta R_2$, **(B)** percent signal change, **(C)** z-score level, **(D)** specificity index, and **(E)** sensitivity index in the M1 region obtained from GE-, SE-, and SAGE-BOLD with three filters. Layer ROIs were obtained from GE-BOLD z-score maps in Supplementary Fig. S3D, and only single-slice iso-depth ROIs were shown. For specificity and sensitivity indices, error bar shows SEM. Solid and shaded lines are mean and SEM across ten subjects. GE BOLD showed the largest sensitivity at the cortical surface, whereas SE and SAGE BOLD using showed the largest sensitivity at ~ 1.0 mm depth, corresponding to the previous studies. For better visualization, the SE BOLD profile was plotted in a different scale. The 46 μm-filter appears to be a good comprise of sensitivity and specificity gain. The 46μm-filter appears to be a good comprise of sensitivity and specificity gain.

Table 2
Laminar specificity, sensitivity indices, and CNR of the primary motor and sensory cortices (mean ± SEM, n = 10 subjects)[a].

Specificity index[b]	Middle / Superficial(M1)	Deeper / Superficial(M1)	Middle / Superficial(S1)	Deeper / Superficial(S1)
GE	0.79 ± 0.03	0.55 ± 0.04	0.70 ± 0.04	0.39 ± 0.05
SE	0.99 ± 0.08	0.62 ± 0.11	1.05 ± 0.08	0.67 ± 0.10
SAGE 27 μm-filter	1.07 ± 0.15	0.71 ± 0.17	1.13 ± 0.09	0.86 ± 0.16
SAGE 46 μm-filter	1.42 ± 0.17	0.81 ± 0.18	1.91 ± 0.32	1.15 ± 0.26
SAGE 62 μm-filter	1.14 ± 0.16	0.57 ± 0.10	1.44 ± 0.24	0.66 ± 0.13

Sensitivity index[c]	Superficial(M1)	Middle(M1)	Deeper(M1)	Superficial(S1)	Middle(S1)	Deeper(S1)
GE	3.24 ± 0.36	2.62 ± 0.22	3.27 ± 0.57	3.00 ± 0.29	2.33 ± 0.27	2.35 ± 0.53
SE	1	1	1	1	1	1
SAGE 27 μm-filter	1.07 ± 0.05	1.10 ± 0.04	1.10 ± 0.06	1.01 ± 0.01	1.08 ± 0.03	1.12 ± 0.14
SAGE 46 μm-filter	1.49 ± 0.14	1.86 ± 0.09	1.60 ± 0.15	1.29 ± 0.09	1.80 ± 0.11	1.67 ± 0.24
SAGE 62 μm-filter	2.32 ± 0.11	2.41 ± 0.15	2.33 ± 0.28	1.92 ± 0.15	2.12 ± 0.13	1.86 ± 0.25

CNR[d]	Superficial(M1)	Middle(M1)	Deeper(M1)	Superficial(S1)	Middle(S1)	Deeper(S1)
GE	9.02 ± 1.19	6.85 ± 1.00	4.57 ± 0.80	10.01 ± 1.33	7.32 ± 1.41	5.84 ± 2.59
SE	2.51 ± 0.30	2.58 ± 0.42	1.54 ± 0.30	2.53 ± 0.31	2.27 ± 0.17	1.39 ± 0.23
SAGE 27 μm-filter	2.79 ± 0.49	2.88 ± 0.46	1.71 ± 0.32	2.55 ± 0.32	2.42 ± 0.16	1.67 ± 0.26
SAGE 46 μm-filter	4.38 ± 0.97	5.28 ± 0.77	2.68 ± 0.54	3.94 ± 1.03	4.87 ± 0.46	2.91 ± 0.47
SAGE 62 μm-filter	7.21 ± 1.40	6.61 ± 0.72	3.89 ± 0.83	6.16 ± 1.15	6.20 ± 0.70	3.46 ± 0.58

[a] Cortical layers were defined as superficial (0–0.75 mm from the surface), middle (0.75–1.50 mm) and deeper (1.50–2.25 mm) layers. Gradient-echo (GE), spin-echo (SE), spin and gradient echo (SAGE) BOLD with three different vessel-size filters were evaluated.
[b] Specificity was determined by percent changes divided by that of the superficial layer; the higher is more specific to microvessels.
[c] Sensitivity index was calculated by z-scores normalized by that of SE BOLD.
[d] Contrast-to-noise ratio (CNR) was calculated by averaged signal changes induced by stimulation divided by baseline standard deviations.

clearly visualize CSF, gray matter, and white matter (the first row). Layers for M1 and S1 were drawn and overlaid on anatomical images (the second row). The anterior and posterior gray matter banks of the central sulcus correspond to M1 and S1, respectively. For the GE-BOLD signal (the third row), the z-score values peak at or nearby the cortical surface near high-intensity CSF region. However, for the SE-BOLD signal (the fourth row), regions of M1 and S1 activation areas are clearly distinguished without significant activation near or in the CSF. SAGE BOLD (the fifth row) shows higher sensitivity than SE BOLD while maintaining spatial specificity. These observations are consistent across all participants.

4. Discussion

By combining GE- and SE-BOLD signals according to vessel-size index, we successfully increased sensitivity and specificity of laminar BOLD-fMRI. We achieved this by designing low-pass filters based on vessel-size-sensitive $\Delta R_2^*/\Delta R_2$ values to retain specific microvascular signals and remove non-specific macrovascular signals of GE-BOLD responses. The SAGE-BOLD fMRI with 0.8 mm isotropic resolution resulted in improved functional sensitivity compared to SE BOLD and higher spatial specificity compared to GE BOLD. Our approach is simple can be easily applied to studies investigating human mesoscopic functional units.

4.1. Vessel-size-sensitive filters

It has been long known from numerical simulations that $\Delta R_2^*/\Delta R_2$ increases with vessel diameter (Fig. 1B) and is often used as a vessel size index (Kiselev et al., 2005; Troprès et al., 2001). However, the exact relationship between vascular diameter and $\Delta R_2^*/\Delta R_2$ is dependent on experimental parameters and magnetic field. Thus, in this study, MC simulations of extravascular BOLD effects were performed for our experimental conditions. Our assumption is that extravascular BOLD effect is dominant, while intravascular BOLD signal is minimal. This condition is valid only when TE is much longer than blood T_2/T_2^* and is met for ultrahigh field fMRI studies at ≥ 7 T (Duong et al., 2002; Lee et al., 1999; Yacoub et al., 2001).

Based on the relationship between vascular diameter and extravascular $\Delta R_2^*/\Delta R_2$, we designed three filters with different cutoff diameters. For the vessel-size-sensitive filter, both diameter at 50% sensitivity ($D_{1/2}$) and transition slope (0.6) are critical to determine pass ($\alpha >$ 0.9) and rejection diameter ($\alpha <$ 0.1). For our designed filters, the pass diameter was set to 27 μm, 46 μm, and 62 μm, respectively, while the transition diameter range corresponded to α of 0.9 to 0.1 was 10–20 μm. If the transition slope is lower, then a larger transition diameter range is obtained. Our vessel-size-sensitive filter was designed for humans and cannot simply translate to different species due to different diameters of intra-cortical ascending and pial veins (e.g., ascending venous diameter in mouse of ~ 9 μm (Blinder et al., 2013)).

We found that the 46 μm-filter selectively enhances BOLD signals from vessel types 1-2 (diameter ≤ 45 μm). The majority of activated voxels in GE-BOLD maps had vessel type 1 in voxel-wise $\Delta R_2^*/\Delta R_2$ values (diameter ≤ 30 μm) (Fig. 3). However, laminar-dependent $\Delta R_2^*/\Delta R_2$ values were mostly composed of vessel type 2 to 3 (Fig. 5A), which can be explained by weighted averaging of iso-depth voxels with various $\Delta R_2^*/\Delta R_2$ values containing also intracortical vessel group V4 with an average diameter of 65 μm. Thus, the 46 μm- and 65 μm-filters, not the 27μm-filter, are to be preferred for laminar fMRI studies because $\Delta R_2^*/\Delta R_2$ values were mostly composed of vessel type 2 to 3 in middle to deeper layers.

Our filter design is based on a single-vessel size. Although vessels with different sizes typically present within a voxel, a single filter function was designed by utilizing the weighted VSI on a voxel or layer basis. Voxels or layers with smaller average vessel size are relatively enhanced compared to those with larger average vessel size, resulting in improvement of spatial specificity. Note that when the composition of vascular sizes is smaller across voxels (e.g., low spatial resolution) or regions, then this approach is ineffective, as the fMRI signal of all voxels or regions will be similarly enhanced or suppressed. Thus, a higher spatial

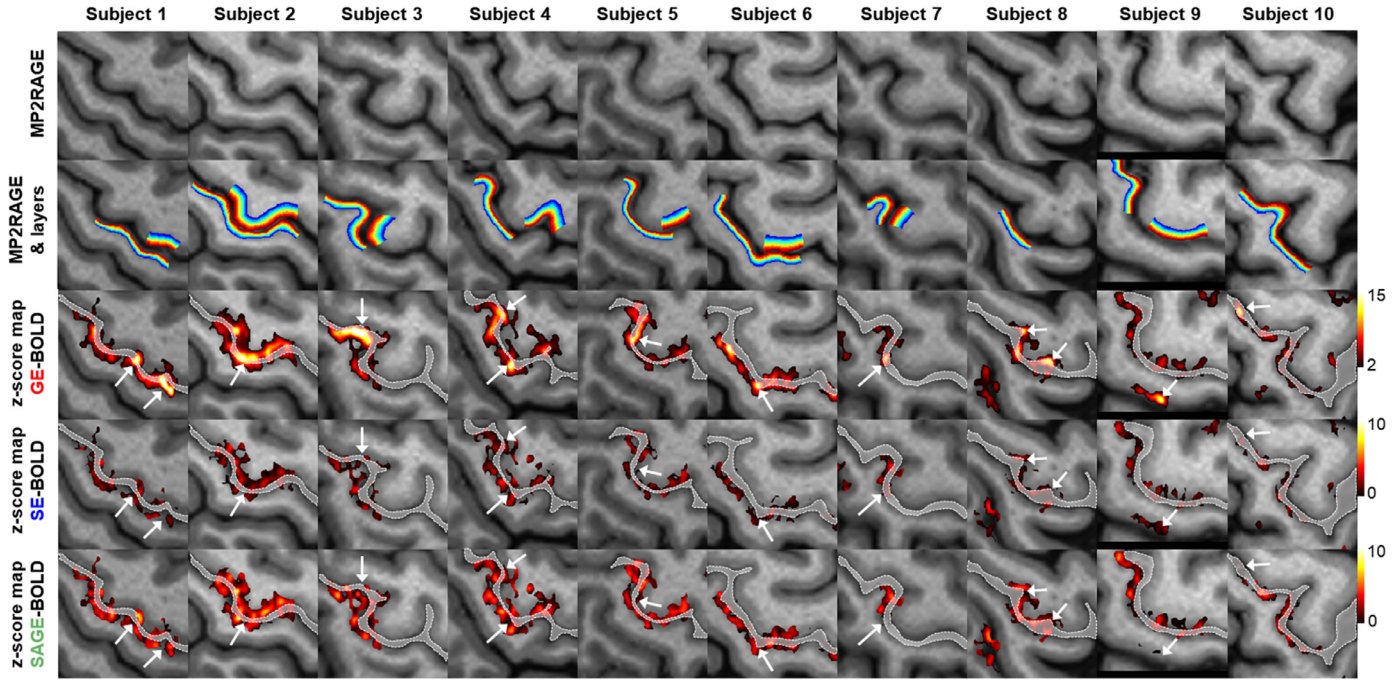

Fig. 7. Functional maps of SAGE-BOLD fMRI with the 46μm-filter vs. SE- and GE-BOLD fMRI. For illustration, one slice was selected for each subject in all 10 subjects. Based on the anatomical images of MP2RAGE (the first row), cortical depth ROIs (colored contours in the second row), as well as the boundary of CSF area (white dashed lines), were drawn. GE- (the third row), SE- (the fourth row), and SAGE-BOLD using the 46 μm-filter z-score maps (the fifth row) were shown. White arrows indicate large vessel areas.

resolution is needed for our approach to be effective: with higher spatial resolution, voxels/layers vary in their vessel sizes and therefore filtering can improve the spatial specificity. It should be noted that filtering of one averaged layer signal (average of multiple iso-depth voxels) is not the same as a sum of filtered signals from multiple voxels within the same layer due to the non-linear mathematical operation. Nevertheless, at even a higher resolution, the noise level may be too large and sensitivity too decreased, and the errors of a filter function and the filtered signals are consequently increased. Thus, a choice of spatial resolution should carefully consider both spatial distribution of vascular density and fMRI signal sensitivity.

An average distance between neighboring intracortical veins in humans is 0.75–1 mm for groups 2 to 3, and 1–4 mm group 5 (Duvernoy et al., 1981; Uludağ and Blinder, 2018). Thus, the spatial resolution should be higher than the inter-vessel distance of group 5 veins, as in the current study (a 0.8mm isotropic spatial resolution). In laminar resolution studies, depth-dependent spatial resolution is preserved, while the sensitivity is gained by averaging of iso-depth signals.

4.2. Property of SAGE-EPI technique

To achieve reasonable TE of SE BOLD using SAGE-EPI sequence, TE of GE BOLD should be minimized because of EPI readout implementation between 90° and 180° pulses for GE BOLD, which can result in reduced sensitivity of GE BOLD compared to GE BOLD acquisition with TE = T_2^* of the tissue. In a similar manner, TE of SE BOLD may not be optimal due to the necessity of prior GE-EPI data collection. Also, the slice coverage of SAGE EPI is inherently narrower than that of conventional SE EPI because of the insertion of EPI readout between 90° and 180° pulses. Similar to SE EPI, achieving high spatiotemporal resolution is difficult mainly due to its long TR and elevated SAR from high flip angle pulses. On the other hand, the SAGE-EPI sequence acquires both SE and GE BOLD within the same TR. The major advantage of this technique is to reduce the total required experiment time and motion artifacts and to simplify co-registration between the GE- and SE-BOLD images. Also, the slice coverage of SAGE EPI was the same as that of SE EPI with reduced EPI readout length by implementing multi-shot approach in this study.

4.3. Experimental determination of $\Delta R_2^*/\Delta R_2$ and application to SAGE BOLD

Accurate $\Delta R_2^*/\Delta R_2$ estimation is important to utilize vessel-size-sensitive filters, which can be used for any fMRI applications to remove macrovascular contributions. To obtain voxel-wise $\Delta R_2^*/\Delta R_2$ from high-resolution fMRI, simultaneous SE- and GE-BOLD data acquisition is required for effective averaging and precise co-registration between SE- and GE-BOLD data. Also, small ΔR_2 values due to the low percent signal change of SE-BOLD signal can cause large errors in $\Delta R_2^*/\Delta R_2$. For example, in case that SE-BOLD signal is noisy in a voxel with microvessels, the estimated $\Delta R_2^*/\Delta R_2$ can be erroneously large. Substantial signal averaging would be necessary to obtain robust ΔR_2 values from SAGE BOLD. Meanwhile, separate GE-BOLD and SE-BOLD measurements are not viable, especially at high spatial resolution fMRI, as extensive repetitions are required to obtain sufficient signal-to-noise ratio (SNR), potentially increasing susceptibility to head motion artifact.

In this study, isotropic resolution GE and SE BOLD were obtained, then vessel-size-sensitive filters were applied on a layer-by-layer basis. Ideally, the filter function applied first to obtain SAGE on a voxel-by-voxel basis, then cortical profile should be obtained. However, due to low SNR of SE BOLD, erroneously large VSI values were observed in the middle and deep cortical layers. To avoid quantification errors by voxel-wise filtering and to enhance the sensitivity of cortical responses, vessel-size-sensitive filters were applied to GE BOLD in layer-wise.

For depth-dependent laminar studies with high registration accuracy, GE- and SE-BOLD fMRI may be measured separately in the same subject, and layer-dependent $\Delta R_2^*/\Delta R_2$ values of targeted cerebral cortex regions can be determined for the same task or different stimulus. Assuming that $\Delta R_2^*/\Delta R_2$ reflects heterogeneity in cerebral vasculature diameter, it can be determined during hypercapnic or hyperoxic stim-

uli (e.g., CO_2 challenge or breath-holding). Then, the layer-dependent vessel-size-sensitive filter determined from experimental $\Delta R_2^*/\Delta R_2$ values would be readily applicable to conventional GE-BOLD fMRI in the same brain region responding to sensory or cognitive stimuli. By using this approach, we can avoid scanning low-sensitive SE-EPI for all fMRI runs in the same subject, and effectively reduce macrovascular contributions to GE-BOLD signals (Fig. 1D). As an example, Supplementary Fig. S5 showed the feasibility of the application of layer-dependent three different filters ($\Delta R_2^*/\Delta R_2$ values) to GE-BOLD data alone. Note that the sensitivity of GE^{α}-BOLD would be the same as that of GE-BOLD, but with the advantage of suppressing high percent signal change at the cortical surface.

In principle, TE of GE BOLD can be different for VSI and functional studies. To obtain GE and SE data simultaneously for VSI measurements, TE should be as short as possible. For fMRI studies, TE of GE BOLD should be optimized for maximal functional sensitivity. To show the feasibility of vessel-size-sensitive filters to conventional GE-BOLD signal, the GE-BOLD signal obtained by changing TE from 18 to 30 ms using MC simulation. And three filters designed for this study were applied to those simulated signal in Supplementary Fig. S6. It showed the selective filtering was effective for each filter; the 27 μm-filter enhanced vessel type 1 and suppressed vessel types 2-4, the 46 μm-filter enhanced vessel types 1-2 (diameter $\leq$ 45 μm) and suppressed vessel types 3-4, the 62 μm-filter enhanced vessel types 1-3 and suppressed vessel type 4.

There are limitations and issues of utilizing vessel-size-sensitive filters: 1) The SAGE-BOLD signal is a composite signal that combines the GE-BOLD signal scaled with a vessel-size-sensitive filter (α) with the SE-BOLD signal. As afore-mentioned, high spatial resolution is needed. 2) The filter function was based on the SE and GE BOLD data. Even if significant microvascular contribution to GE BOLD signals exists in superficial layers, the filter function α of $\sim$ 0.0 (see Fig. 1) suppresses the microvascular GE BOLD contribution to the combined SAGE data. Consequently, the SAGE response in superficial layers is relatively less gained than that in middle and deep layers, compared to the SE BOLD response (see SAGE vs. SE profile in Figs.5B and 6B). 3) The noise level of the combined SAGE-BOLD signal is elevated by the non-linear multiplication of the GE- and SE-BOLD signals. When α increases as the filter tuning diameter increases, both functional signal change and baseline fluctuation increase (Supplementary Table S1). Consequently, the CNR of SAGE-BOLD with the three filters is higher than that of SE BOLD only, which is thought to be due to a larger increase in functional signal changes than noises as shown in Table 2. Thus, the filter application is its current form can be helped to task-based analysis utilizing as z-scores or percent signal changes. However, even though vessel size filtering is a general method, for neuroscience data analysis such as resting-state connectivity and multivariate analyses etc., vessel size filtering may have to be adapted and further validated.

4.4. Comparison with existing specific high-resolution fMRI methods

In SE-fMRI studies, we previously showed better sensitivity by averaging two SEs than conventional SE BOLD (Han et al., 2021). This approach may be susceptible to specific absorption rate (SAR) limitation due to the two 180° pulses utilized, resulting in a smaller slice coverage than conventional SE BOLD. On the other hand, the proposed SAGE EPI can have better slice coverage than dSE EPI because SAGE-EPI sequence has the same radiofrequency (RF) pulse pair of 90–180° as the conventional SE EPI. Moreover, compared to SE BOLD, dSE BOLD increased the functional sensitivity by 14%, whereas the functional sensitivity index in the vessel type 1-2 by SAGE BOLD was observed to be enhanced by a factor of ~1.38 to ~1.84 (Fig. 4E). Additionally, the laminar profiles of sensitivity index normalized by SE BOLD were compared in Supplementary Fig. S7. As shown in Table 2, SAGE BOLD with 46-μm filter showed 86% and 80% sensitivity gain at middle layers in M1 and S1 areas, respectively when compared with SE BOLD.

To improve spatial specificity, non-BOLD contrasts such as cerebral blood flow (CBF) and CBV-based methods, are increasingly being utilized because of their sensitivity to microvasculature. Arterial spin labeling (ASL) maps CBF by using RF pulses to label inflowing water in the arterial blood, but the estimated temporal SNR (tSNR) of laminar CBF at 0.7 mm isotropic resolution is expected to be 10–20% of that of GE-BOLD fMRI (Huber et al., 2019; Kashyap et al., 2021). VASO uses an inversion recovery sequence to exploit the T_1 difference between blood and surrounding tissue to negate the blood signal, and the CNR of VASO is approximately 40–70% of that of GE-BOLD fMRI (Huber et al., 2019). On the other hand, confounding factors such as blood T_1 uncertainty and perfusion/CSF contaminations are susceptible by user-defined parameters, limiting wide availability of the CBV-based VASO method (Huber et al., 2019). Especially, there is limiting TR in using VASO (minimal TR $\sim$ 2.1 s at 7 T as blood T_1) because VASO is weighted by the T_1-based contrast. On the other hand, since SAGE BOLD is similar to standard SE BOLD, TR can be reduced by the reduction of the slice coverage.

5. Conclusions

SAGE-EPI sequence was implemented to obtain high specificity and sensitivity by utilizing a vessel-size-sensitive filter to the GE-BOLD signal, which reduces macrovascular contributions, and to combine retained microvascular GE BOLD with the SE-BOLD signals. To investigate our proposed idea, fMRI with 0.8mm isotropic resolution was performed on the primary motor and sensory cortices in humans at 7 T and showed improved laminar specificity and sensitivity and is therefore an excellent tool for high spatial resolution UHF-fMRI studies for resolving mesoscopic functional units.

Data and code availability statements

All fMRI data analyzed in our study will be available by request. Raw data will be available by request and a data sharing agreement.

Credit authorship contribution statement

SoHyun Han: Conceptualization, Methodology, Software, Validation, Writing – review & editing. **Seulgi Eun:** Data curation. **HyungJoon Cho:** Conceptualization, Writing – review & editing. **Kamil Uludağ:** Conceptualization, Supervision, Writing – review & editing. **Seong-Gi Kim:** Conceptualization, Supervision, Writing – review & editing, Funding acquisition.

Acknowledgments

This work was supported by Institute for Basic Science in Korea (IBS-R015-D1).

Supplementary materials

Supplementary material associated with this article can be found, in the online version, at doi:10.1016/j.neuroimage.2022.119675.

References

Báez-Yánez, M.G., Ehses, P., Mirkes, C., Tsai, P.S., Kleinfeld, D., Scheffler, K., 2017. The impact of vessel size, orientation and intravascular contribution on the neurovascular fingerprint of BOLD bSSFP fMRI. Neuroimage 163, 13–23. doi:10.1016/j.neuroimage.2017.09.015.

Blinder, P., Tsai, P.S., Kaufhold, J.P., Knutsen, P.M., Suhl, H., Kleinfeld, D., 2013. The cortical angiome: an interconnected vascular network with noncolumnar patterns of blood flow. Nat. Neurosci. 16, 889–897. doi:10.1038/nn.3426.

Boxerman, J.L., Hamberg, L.M., Rosen, B.R., Weisskoff, R.M., 1995. Mr contrast due to intravascular magnetic susceptibility perturbations. Magn. Reson. Med. 34, 555–566. doi:10.1002/mrm.1910340412.

Budde, J., Shajan, G., Zaitsev, M., Scheffler, K., Pohmann, R., 2014. Functional MRI in human subjects with gradient-echo and spin-echo EPI at 9.4 T. Magn. Reson. Med. 71, 209–218. doi:10.1002/mrm.24656.

Cheng, K., Waggoner, R.A., Tanaka, K., 2001. Human ocular dominance columns as revealed by high-field functional magnetic resonance imaging. Neuron 32, 359–374. doi:10.1016/S0896-6273(01)00477-9.

Curtis, A.T., Hutchison, R.M., Menon, R.S., 2014. Phase based venous suppression in resting-state BOLD GE-fMRI. Neuroimage 100, 51–59. doi:10.1016/j.neuroimage.2014.05.079.

De Martino, F., Yacoub, E., Kemper, V., Moerel, M., Uludag, K., De Weerd, P., Ugurbil, K., Goebel, R., Formisano, E., 2018. The impact of ultra-high field MRI on cognitive and computational neuroimaging. Neuroimage 168, 366–382. doi:10.1016/j.neuroimage.2017.03.060.

Donahue, K.M., Krouwer, H.G.J., Rand, S.D., Pathak, A.P., Marszalkowski, C.S., Censky, S.C., Prost, R.W., 2000. Utility of simultaneously acquired gradient-echo and spin-echo cerebral blood volume and morphology maps in brain tumor patients. Magn. Reson. Med. 43, 845–853. doi:10.1002/1522-2594(200006)43:6<845::AID-MRM10>3.0.CO;2-J.

Donahue, K.M., Van Kylen, J., Guven, S., El-Bershawi, A., Luh, W.M., Bandettini, P.A., Cox, R.W., Hyde, J.S., Kissebah, A.H., 1998. Simultaneous gradient-echo/spin-echo EPI of graded ischemia in human skeletal muscle. J. Magn. Reson. Imaging 8, 1106–1113. doi:10.1002/jmri.1880080516.

Dumoulin, S.O., Fracasso, A., van der Zwaag, W., Siero, J.C.W., Petridou, N., 2018. Ultra-high field MRI: advancing systems neuroscience towards mesoscopic human brain function. Neuroimage 168, 345–357. doi:10.1016/j.neuroimage.2017.01.028.

Duong, T.Q., Yacoub, E., Adriany, G., Hu, X., Ugurbil, K., Vaughan, J.T., Merkle, H., Kim, S.G., 2002. High-resolution, spin-echo BOLD, and CBF fMRI at 4 and 7 T. Magn. Reson. Med. 48, 589–593. doi:10.1002/mrm.10252.

Duvernoy, H.M., Delon, S., Vannson, J.L., 1981. Cortical blood vessels of the human brain. Brain Res. Bull. 7, 519–579. doi:10.1016/0361-9230(81)90007-1.

Emblem, K.E., Mouridsen, K., Bjornerud, A., Farrar, C.T., Jennings, D., Borra, R.J.H., Wen, P.Y., Ivy, P., Batchelor, T.T., Rosen, B.R., Jain, R.K., Sorensen, A.G., 2013. Vessel architectural imaging identifies cancer patient responders to anti-angiogenic therapy. Nat. Med. 19, 1178–1183. doi:10.1038/nm.3289.

Fischl, B., Dale, A.M., 2000. Measuring the thickness of the human cerebral cortex from magnetic resonance images. Proc. Natl. Acad. Sci. USA 97, 11050–11055. doi:10.1073/pnas.200033797.

Fracasso, A., Luijten, P.R., Dumoulin, S.O., Petridou, N., 2018. Laminar imaging of positive and negative BOLD in human visual cortex at 7 T. Neuroimage 164, 100–111. doi:10.1016/j.neuroimage.2017.02.038.

Frahm, J., Merboldt, K.D., Hänicke, W., Kleinschmidt, A., Boecker, H., 1994. Brain or vein–oxygenation or flow? On signal physiology in functional MRI of human brain activation. NMR Biomed. 7, 45–53. doi:10.1002/nbm.1940070108.

Goense, J.B.M., Logothetis, N.K., 2006. Laminar specificity in monkey V1 using high-resolution SE-fMRI. Magn. Reson. Imaging 24, 381–392. doi:10.1016/j.mri.2005.12.032.

Goodyear, B.G., Menon, R.S., 2001. Brief visual stimulation allows mapping of ocular dominance in visual cortex using fMRI. Hum. Brain Mapp. 14, 210–217. doi:10.1002/hbm.1053.

Han, S., Eun, S., Cho, H., Uludağ, K., Kim, S.-G., 2021. Improvement of sensitivity and specificity for laminar BOLD fMRI with double spin-echo EPI in humans at 7 T. Neuroimage 241, 118435. doi:10.1016/j.neuroimage.2021.118435.

Harel, N., Lin, J., Moeller, S., Ugurbil, K., Yacoub, E., 2006. Combined imaging-histological study of cortical laminar specificity of fMRI signals. Neuroimage 29, 879–887. doi:10.1016/j.neuroimage.2005.08.016.

Harmer, J., Sanchez-Panchuelo, R.M., Bowtell, R., Francis, S.T., 2012. Spatial location and strength of BOLD activation in high-spatial-resolution fMRI of the motor cortex: A comparison of spin echo and gradient echo fMRI at 7T. NMR Biomed. 25, 717–725. doi:10.1002/nbm.1783.

Havlicek, M., Uludağ, K., 2020. A dynamical model of the laminar BOLD response. Neuroimage 204. doi:10.1016/j.neuroimage.2019.116209.

Heinzle, J., Koopmans, P.J., den Ouden, H.E.M., Raman, S., Stephan, K.E., 2016. A hemodynamic model for layered BOLD signals. Neuroimage 125, 556–570. doi:10.1016/j.neuroimage.2015.10.025.

Hillman, E.M.C., 2014. Coupling mechanism and significance of the BOLD signal: a status report. Annu. Rev. Neurosci. doi:10.1146/annurev-neuro-071013-014111.

Huber, L., Finn, E.S., Handwerker, D.A., Bönstrup, M., Glen, D.R., Kashyap, S., Ivanov, D., Petridou, N., Marrett, S., Goense, J., Poser, B.A., Bandettini, P.A., 2020. Sub-millimeter fMRI reveals multiple topographical digit representations that form action maps in human motor cortex. Neuroimage 208, 116463. doi:10.1016/j.neuroimage.2019.116463.

Huber, L., Goense, J., Kennerley, A.J., Trampel, R., Guidi, M., Reimer, E., Ivanov, D., Neef, N., Gauthier, C.J., Turner, R., Möller, H.E., 2015. Cortical lamina-dependent blood volume changes in human brain at 7T. Neuroimage 107, 23–33. doi:10.1016/j.neuroimage.2014.11.046.

Huber, L., Handwerker, D.A., Jangraw, D.C., Chen, G., Hall, A., Stüber, C., Gonzalez-Castillo, J., Ivanov, D., Marrett, S., Guidi, M., Goense, J., Poser, B.A., Bandettini, P.A., 2017. High-resolution CBV-fMRI allows mapping of laminar activity and connectivity of cortical input and output in human M1. Neuron 96. doi:10.1016/j.neuron.2017.11.005, 1253-1263. e7.

Huber, L., Uludağ, K., Möller, H.E., 2019. Non-BOLD contrast for laminar fMRI in humans: CBF, CBV, and CMRO2. Neuroimage doi:10.1016/j.neuroimage.2017.07.041.

Jain, V., Abdulmalik, O., Propert, K.J., Wehrli, F.W., 2012. Investigating the magnetic susceptibility properties of fresh human blood for noninvasive oxygen saturation quantification. Magn. Reson. Med. 68, 863–867. doi:10.1002/mrm.23282.

Kashyap, S., Ivanov, D., Havlicek, M., Huber, L., Poser, B.A., Uludağ, K., 2021. Sub-millimetre resolution laminar fMRI using Arterial Spin Labelling in humans at 7 T. PLoS One 16, e0250504. doi:10.1371/journal.pone.0250504.

Kay, K., Jamison, K.W., Zhang, R.Y., Uğurbil, K., 2020. A temporal decomposition method for identifying venous effects in task-based fMRI. Nat. Methods 17, 1033–1039. doi:10.1038/s41592-020-0941-6.

Kim, S.G., Fukuda, M., 2008. Lessons from fMRI about mapping cortical columns. Neuroscientist doi:10.1177/1073858407309541.

Kim, SG, Hendrich, K., Hu, X., Merkle, H., Ugurbil, K., 1994. Potential pitfalls of functional MRI using conventional gradient-recalled echo techniques. NMR Biomed. 7, 69–74.

Kiselev, V.G., Strecker, R., Ziyeh, S., Speck, O., Hennig, J., 2005. Vessel size imaging in humans. Magn. Reson. Med. 53, 553–563. doi:10.1002/mrm.20383.

Lawrence, S.J.D., Formisano, E., Muckli, L., de Lange, F.P., 2019. Laminar fMRI: Applications for cognitive neuroscience. Neuroimage doi:10.1016/j.neuroimage.2017.07.004.

Lee, A.T., Glover, G.H., Meyer, C.H., 1995. Discrimination of large venous vessels in time-course spiral blood-oxygen-level-dependent magnetic-resonance functional neuroimaging. Magn. Reson. Med. 33, 745–754. doi:10.1002/mrm.1910330602.

Lee, D., Le, T.T., Im, G.H., Kim, S.-G., 2022. Whole-brain perfusion mapping in mice by dynamic BOLD MRI with transient hypoxia. J. Cereb. blood flow Metab. Off. J. Int. Soc. Cereb. Blood Flow Metab doi:10.1177/0271678X221117008, 271678×221117008..

Lee, S.-P., Silva, A.C., Ugurbil, K., Kim, S.-G., 1999. Diffusion-weighted spin-echo fMRI at 9.4 T: microvascular/tissue contribution to BOLD signal changes. Magn. Reson. Med. 42, 919–928. doi:10.1002/(SICI)1522-2594(199911)42:5<919::AID-MRM12>3.0.CO;2-8.

Manhard, M.K., Bilgic, B., Liao, C., Han, S.H., Witzel, T., Yen, Y.F., Setsompop, K., 2019. Accelerated whole-brain perfusion imaging using a simultaneous multislice spin-echo and gradient-echo sequence with joint virtual coil reconstruction. Magn. Reson. Med. 82, 973–983. doi:10.1002/mrm.27784.

Markuerkiaga, I., Barth, M., Norris, D.G., 2016. A cortical vascular model for examining the specificity of the laminar BOLD signal. Neuroimage 132, 491–498. doi:10.1016/j.neuroimage.2016.02.073.

Marquardt, I., Schneider, M., Gulban, O.F., Ivanov, D., Uludağ, K., 2018. Cortical depth profiles of luminance contrast responses in human V1 and V2 using 7 T fMRI. Hum. Brain Mapp. 39, 2812–2827. doi:10.1002/hbm.24042.

Marques, J.P., Kober, T., Krueger, G., van der Zwaag, W., Van de Moortele, P.F., Gruetter, R., 2010. MP2RAGE, a self bias-field corrected sequence for improved segmentation and T1-mapping at high field. Neuroimage 49, 1271–1281. doi:10.1016/j.neuroimage.2009.10.002.

Masamoto, K., Kurachi, T., Takizawa, N., Kobayashi, H., Tanishita, K., 2004. Successive depth variations in microvascular distribution of rat somatosensory cortex. Brain Res. 995, 66–75. doi:10.1016/j.brainres.2003.09.055.

Menon, R.S., 2002. Postacquisition suppression of large-vessel BOLD signals in high-resolution fMRI. Magn. Reson. Med. 47, 1–9. doi:10.1002/mrm.10041.

Menon, R.S., Ogawa, S., Tank, D.W., Uğurbil, K., 1993. 4 Tesla gradient recalled echo characteristics of photic stimulation-induced signal changes in the human primary visual cortex. Magn. Reson. Med. 30, 380–386. doi:10.1002/mrm.1910300317.

Menon, R.S., Thomas, C.G., Gati, J.S., 1997. Investigation of BOLD contrast in fMRI using multi-shot EPI. NMR Biomed. 10, 179–182. doi:10.1002/(SICI)1099-1492(199706/08)10:4/5<179::AID-NBM463>3.0.CO;2-X.

Moon, C.H., Fukuda, M., Park, S.H., Kim, S.G., 2007. Neural interpretation of blood oxygenation level-dependent fMRI maps at submillimeter columnar resolution. J. Neurosci. 27, 6892–6902. doi:10.1523/JNEUROSCI.0445-07.2007.

Ogawa, S., Menon, R.S., Tank, D.W., Kim, S.G., Merkle, H., Ellermann, J.M., Ugurbil, K., 1993. Functional brain mapping by blood oxygenation level-dependent contrast magnetic resonance imaging. A comparison of signal characteristics with a biophysical model. Biophys. J. 64, 803–812. doi:10.1016/S0006-3495(93)81441-3.

Olman, C.A., Harel, N., Feinberg, D.A., He, S., Zhang, P., Ugurbil, K., Yacoub, E., 2012. Layer-specific fmri reflects different neuronal computations at different depths in human V1. PLoS One 7. doi:10.1371/journal.pone.0032536.

Olman, C.A., Inati, S., Heeger, D.J., 2007. The effect of large veins on spatial localization with GE BOLD at 3 T: Displacement, not blurring. Neuroimage 34, 1126–1135. doi:10.1016/j.neuroimage.2006.08.045.

Oshio, K., Feinberg, D.A., 1991. GRASE (Gradient-and Spin-Echo) imaging: a novel fast MRI technique. Magn. Reson. Med. 20, 344–349. doi:10.1002/mrm.1910200219.

Pathak, A.P., Ward, B.D., Schmainda, K.M., 2008. A novel technique for modeling susceptibility-based contrast mechanisms for arbitrary microvascular geometries: the finite perturber method. Neuroimage 40, 1130–1143. doi:10.1016/j.neuroimage.2008.01.022.

Polimeni, J.R., Fischl, B., Greve, D.N., Wald, L.L., 2010. Laminar analysis of 7T BOLD using an imposed spatial activation pattern in human V1. Neuroimage 52, 1334–1346. doi:10.1016/j.neuroimage.2010.05.005.

Schmiedeskamp, H., Straka, M., Newbould, R.D., Zaharchuk, G., Andre, J.B., Olivot, J.M., Moseley, M.E., Albers, G.W., Bammer, R., 2012. Combined spin- and gradient-echo perfusion-weighted imaging. Magn. Reson. Med. 68, 30–40. doi:10.1002/mrm.23195.

Shmuel, A., Yacoub, E., Chaimow, D., Logothetis, N.K., Ugurbil, K., 2007. Spatio-temporal point-spread function of fMRI signal in human gray matter at 7 Tesla. Neuroimage 35, 539–552. doi:10.1016/j.neuroimage.2006.12.030.

Spees, W.M., Yablonskiy, D.A., Oswood, M.C., Ackerman, J.J.H., 2001. Water proton MR properties of human blood at 1.5 Tesla: Magnetic susceptibility, T1, T2*, T2, and non-Lorentzian signal behavior. Magn. Reson. Med. 45, 533–542. doi:10.1002/mrm.1072.

Troprès, I., Grimault, S., Vaeth, A., Grillon, E., Julien, C., Payen, J.F., Lamalle, L., Décorps, M., 2001. Vessel size imaging. Magn. Reson. Med. 45, 397–408. doi:10.1002/1522-2594(200103)45:3<397::AID-MRM1052>3.0.CO;2-3.

Turner, R., 2002. How much codex can a vein drain? Downstream dilution of activation-related cerebral blood oxygenation changes. Neuroimage 16, 1062–1067. doi:10.1006/nimg.2002.1082.

Uludağ, K., Blinder, P., 2018. Linking brain vascular physiology to hemodynamic response in ultra-high field MRI. Neuroimage 168, 279–295. doi:10.1016/j.neuroimage.2017.02.063.

Uludag, K., Havlicek, M., 2021. Determining laminar neuronal activity from BOLD fMRI using a generative model. Prog. Neurobiol. 207, 102055. doi:10.1016/j.pneurobio.2021.102055.

Uludağ, K., Müller-Bierl, B., Uğurbil, K., 2009. An integrative model for neuronal activity-induced signal changes for gradient and spin echo functional imaging. Neuroimage 48, 150–165. doi:10.1016/j.neuroimage.2009.05.051.

Weisskoff, R., Zuo, C.S., Boxerman, J.L., Rosen, B.R., 1994. Microscopic susceptibility variation and transverse relaxation: theory and experiment. Magn. Reson. Med. 31, 601–610. doi:10.1002/mrm.1910310605.

Worsley, K.J., 2001. Statistical analysis of activation images. In: Functional Magnetic Resonance Imaging. Oxford University Press, pp. 251–270. doi:10.1093/acprof:oso/9780192630711.003.0014.

Yacoub, E., Harel, N., Uğurbil, K., 2008. High-field fMRI unveils orientation columns in humans. Proc. Natl. Acad. Sci. USA 105, 10607–10612. doi:10.1073/pnas.0804110105.

Yacoub, E., Shmuel, A., Logothetis, N., Uğurbil, K., 2007. Robust detection of ocular dominance columns in humans using Hahn Spin Echo BOLD functional MRI at 7 Tesla. Neuroimage 37, 1161–1177. doi:10.1016/j.neuroimage.2007.05.020.

Yacoub, E., Shmuel, A., Pfeuffer, J., Van De Moortele, P.F., Adriany, G., Andersen, P., Thomas Vaughan, J., Merkle, H., Ugurbil, K., Hu, X., 2001. Imaging brain function in humans at 7 Tesla. Magn. Reson. Med. 45, 588–594. doi:10.1002/mrm.1080.

Yu, Y., Huber, L., Yang, J., Jangraw, D.C., Handwerker, D.A., Molfese, P.J., Chen, G., Ejima, Y., Wu, J., Bandettini, P.A., 2019. Layer-specific activation of sensory input and predictive feedback in the human primary somatosensory cortex. Sci. Adv. 5. doi:10.1126/sciadv.aav9053.

Zhao, F., Wang, P., Hendrich, K., Ugurbil, K., Kim, S.G., 2006. Cortical layer-dependent BOLD and CBV responses measured by spin-echo and gradient-echo fMRI: Insights into hemodynamic regulation. Neuroimage 30, 1149–1160. doi:10.1016/j.neuroimage.2005.11.013.

Zhao, F., Wang, P., Kim, S.G., 2004. Cortical depth-dependent gradient-echo and spin-echo BOLD fMRI at 9.4T. Magn. Reson. Med. 51, 518–524. doi:10.1002/mrm.10720.